# Study of Rayleigh–Taylor Growth in Directly Driven Cryogenic-Deuterium Targets

## Introduction

In inertial confinement fusion (ICF),[1,2] a spherical capsule is uniformly irradiated to compress a target containing a deuterium–tritium (DT) ice shell, creating the hot-spot temperature and fuel-density conditions required to achieve ignition and significant thermonuclear energy gain. The growth of areal-density ($\rho R$) perturbations resulting from Rayleigh–Taylor[3,4] (RT) instability can compromise the target's integrity, quenching the hot-spot formation prior to achieving thermonuclear ignition.[1,2,5–23] In the linear regime, modulations grow exponentially with a growth rate given by[24]

$$\gamma = \alpha\sqrt{kg\Big/\left(1+kL_\mathrm{m}\right)} - \beta k V_\mathrm{a}\,, \tag{1}$$

where $\alpha$ and $\beta$ are constants, $k$ is the wave number of the modulation, $g$ is the acceleration of the target, $L_\mathrm{m}$ is the density scale length at the ablation front, and $V_\mathrm{a}$ is the ablation velocity. Prior to target acceleration, during shock transit, the ablative Richtmyer–Meshkov (RM) instability causes areal-density modulations to oscillate with an oscillation frequency of[25,26]

$$\omega = k\sqrt{V_\mathrm{b}\cdot V_\mathrm{a}}\,, \tag{2}$$

where $V_\mathrm{b}$ is the blowoff velocity. Direct-drive–ignition designs[27] use a thick cryogenic (cryo)-DT shell encased by a thin (~4-$\mu$m) CH ablator to maximize the amount of fusion fuel contained in the compressed target at peak burn of the implosion.[28] As the thin CH layer is ablated, the implosion hydrodynamics become ablative in DT. Targets with DT ablators are predicted to be more robust to the RT instability than mass-equivalent CH ablators.[24] Reduced density in DT ablators compared to CH increases the ablation velocity, reducing the growth rate while also allowing for thicker ablators without compromising target acceleration and implosion velocity. The ablative stabilization constant $\beta$ [Eq. (1)] is ~1.7 for CH and ~2.6 for DT, providing increased hydrodynamic stability for DT ablators.[24] The growth rate of the RT instability has been measured experimentally under a variety of target and drive conditions for room-temperature materials, such as CH, showing good agreement with theoretical predictions and hydrodynamic simulations at drive intensities up to ~$5 \times 10^{14}$ W/cm$^2$ (Refs. 2,10,12,29,30). Areal-density modulations can be seeded by target defects created during manufacturing and/or nonuniformities in the target driver (laser imprinting). Significant mitigation of laser imprinting is achieved by the use of distributed phase plates (DPP's)[31] and smoothing by spectral dispersion (SSD).[32] To design a target that is robust to RT instability and will achieve thermonuclear ignition, it is essential to understand the evolution of $\rho R$ modulations in cryo DT. This article presents the first experiments that verify hydrodynamic simulations of RT growth in cryo $D_2$ (hydrodynamically equivalent to DT) at conditions relevant to achieving direct-drive thermonuclear ignition with a mass preimposed initial condition. Previous experiments have been performed using intensity-imprinted initial modulations, although they could not be simulated because of software limitations.[33] The following sections describe the experimental design; present the experimental configuration and the experimental results; compare results with simulations; and present conclusions.

## Experimental Design

Laser-driven RT experiments are typically performed in planar geometry using face-on x-ray radiography.[12,12,29,30] A target with a known seed modulation (either preimposed or laser imprinted) is irradiated while a high-$Z$ x-ray backlighter foil is used to image the modulation evolution. Figure 128.9 shows the basic face-on radiography configuration used in most direct-drive planar RT experiments. The drive target is irradiated with overlapping drive beams while x rays from a high-$Z$ backlighter traverse the target and are measured on an x-ray framing camera with an imaging pinhole array.[34] X-ray radiography relies on the attenuation of backlighter x rays (typically greater than 1 keV because of the spectral response of the framing camera) by the drive target such that variations in the target's areal density will be measured as variations in the optical depth of the radiograph. Measuring $\rho R$ modulation evolution in cryo $D_2$ presents two significant challenges to the typical face-on x-ray radiography scheme: $D_2$ has little x-ray attenuation at energies greater than 1 keV and a cryo-$D_2$ layer must be contained by a solid ambient material, typically plas-

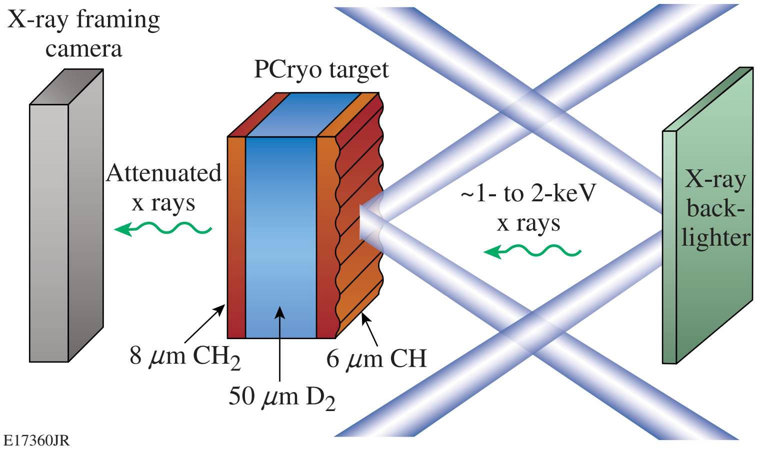

Figure 128.9
Experimental configuration for face-on x-ray radiography. A planar cryogenic (PCryo) target with a sinusoidal seed areal-density modulation is driven by 12 OMEGA drive beams while a backlighter emits 1.3-keV x rays, which are imaged with a time-gated x-ray framing camera. The planar cryogenic drive target consists of a 50-$\mu$m, liquid-$D_2$ layer sandwiched between a 6-$\mu$m-thick front CH window and an 8-$\mu$m-thick rear $CH_2$ window. The entire assembly is held in a 2-$\mu$m-sq Cu washer with a 1.5-mm inner diameter (not pictured) and is cryogenically cooled to ~20 K. The front CH window is seeded with a 60-$\mu$m-wavelength sinusoidal modulation with an initial amplitude of 0.25 $\mu$m, which will imprint into the $D_2$ layer as the window is ablated by the drive beams.

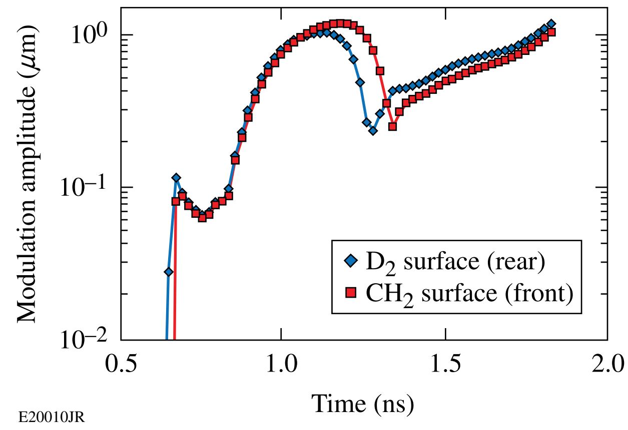

Figure 128.10
Simulated rear-surface modulation for a 50-$\mu$m-thick liquid-$D_2$ target with a 6-$\mu$m-thick modulated front CH window and an 8-$\mu$m-thick rear $CH_2$ window driven by a 2-ns square pulse. The plot shows the modulation amplitude at the back $D_2$ surface (blue diamonds) and the modulation in the rear $CH_2$ window of the target (red squares), indicating that the $CH_2$ window modulation evolution is dominated by feedthrough from the $D_2$ ablation front.

tic (CH). Lower-energy x rays required to directly radiograph the cryo $D_2$ would suffer from severe attenuation in the CH layer and increased background from the soft x rays produced by the CH plasma. Instead, the modulation evolution in $D_2$ is measured indirectly using modulation feedthrough[35] into the rear window of a planar cryo-$D_2$ target. A schematic of the planar cryo-$D_2$ target can be seen in Fig. 128.9. The target consists of a 50-$\mu$m-thick $D_2$ "sandwich" held in place by a 6-$\mu$m-thick front CH window and an 8-$\mu$m-thick rear $CH_2$ window mounted in a 2-mm-sq copper washer with an inner diameter of 1.5 mm. The front CH window is seeded with a 60-$\mu$m-wavelength sinusoidal modulation with an initial amplitude of 0.25 $\mu$m, and the entire assembly is mounted to a cryo finger that cools the target to ~20 K so a liquid-$D_2$ layer exists between the two plastic windows. As the target is driven, the front CH window is ablated away and the modulation evolution at the ablation front is governed by the ablative growth in $D_2$. These $D_2$ modulations feed through to the rear $CH_2$ window of the target with the relationship

$$a_{\mathrm{CH}_2}(k,t) = a_{\mathrm{D}_2}(k,t)e^{-k\cdot d(t)}, \qquad (3)$$

where $\alpha_{\mathrm{D}_2}$ is the modulation amplitude at the $D_2$ ablation front, $\alpha_{\mathrm{CH}_2}$ is the modulation amplitude at the rear $CH_2$ window, $k$ is the modulation wave number, and $d(t)$ is the distance between the $D_2$ ablation front and the rear $CH_2$ window of the target. Equation (3) indicates that the modulation amplitude at the $D_2$ ablation front will always be greater than in the $CH_2$ window. *DRACO*[36] simulations indicate that the modulations in $D_2$ correlate well with the observed modulation on the rear $CH_2$ window. The modulation amplitude at the ablation surface in $D_2$ feeds through to the back $D_2$ surface and is governed by the same feedthrough relation as defined in Eq. (3). Figure 128.10 shows the simulated modulation amplitude evolution at the back $D_2$ surface (blue diamonds) as well as the modulation in the rear $CH_2$ window (red squares) from *DRACO* for a target with a 50-$\mu$m-thick $D_2$ layer held in place by a 6-$\mu$m-thick front CH window and an 8-$\mu$m-thick rear $CH_2$ window with an initial front-surface modulation with an amplitude of 0.25 $\mu$m at a wavelength of 60 $\mu$m being driven by a 2-ns square pulse with an intensity of $4 \times 10^{14}$ W/cm$^2$, showing good correlation between the $D_2$ and $CH_2$ layers.

## Experimental Configuration

The target shown in Fig. 128.9 was irradiated by 12 overlapping UV beams from OMEGA with a spot diameter of ~750 $\mu$m using a 2-ns square pulse at a peak intensity of $4 \times 10^{14}$ W/cm$^2$. The spatial profiles of the beams were smoothed using SSD[32] and DPP's.[31] A uranium backlighter located 9 mm from the drive target was irradiated by ten UV beams with a spot diameter of 1 mm, creating x-ray radiographs on a time-gated x-ray framing camera[34] filtered with 1 $\mu$m of Al with an additional 3-$\mu$m-Al blast shield located 4.5 mm from the drive target to prevent preheating of the target by soft x rays. This configuration yielded a peak x-ray energy of ~1.3 keV to radiograph the front and rear plastic windows of the target. The framing camera captured eight radiographs with a temporal resolution of ~80 ps and a spatial resolution of ~10 $\mu$m. Data were extracted from five radiographs from 0.8 to 1.6 ns.

A Weiner filter was constructed to extract the signal from the noise from each individual image.[37] The true signal was reconstructed only from data with spatial frequencies near 16.6 mm$^{-1}$, corresponding to the 60-$\mu$m-wavelength seed modulation. For each image, the noise was approximated by the lineout perpendicular to the seed modulation. The noise for all of the images was compared to ensure that the noise spectrum was not changing significantly during the target drive, which would indicate true broadband modulation growth and not noise. Figure 128.11 shows a filtered 300-$\mu$m-sq radiograph taken at 1.25 ns into the drive.

The two-dimensional (2-D) hydrodynamics code *DRACO*[36] simulated the modulation evolution using flux-limited local electron transport, where the heat flux is taken as the smaller of the *Spitzer–Härm heat flux*[38] and the *flux-limited free-streaming heat flux*,[39] with a standard flux limiter of $f = 0.06$. The simulation used *SESAME* 5263 (Ref. 40) for the equation of state (EOS) of the cryogenic-$D_2$ layer. Figure 128.12 shows the temperature and pressure profiles of the $D_2$ shock front from *DRACO*. The simulated shocked $D_2$ density reaches 3 to $4\times$ the initial liquid-$D_2$ density (0.171 g/cc) with pressures ranging from 15 to 25 Mbar and temperatures from 20 to 30 eV during the shock transit into the $D_2$ liquid. Multiple shocks and rarefactions traverse the target prior to the onset of target acceleration caused by the multiple interfaces. At 0.8 ns, the $D_2$ layer achieves its peak pressure of 65 Mbar at a temperature of 50 eV because of the rarefaction wave heating from the rear $CH_2$ window. For these conditions, *SESAME* 5263 is in good agreement with the first principles EOS (FPEOS) for $D_2$ calculated by S. X. Hu *et al.*[41]

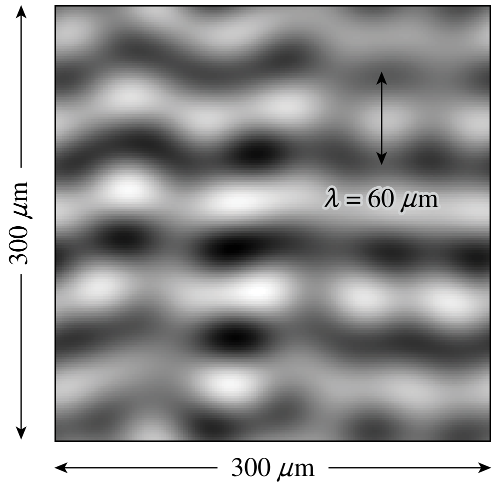

Figure 128.11
A Weiner-filtered, 300-$\mu$m-sq face-on radiograph for the planar-cryogenic-$D_2$ target in Fig. 128.9 driven by 12 drive beams with a 2-ns square pulse with a peak overlapped intensity of $4 \times 10^{14}$ W/cm$^2$ taken at 1.25 ns. The 60-$\mu$m wavelength appears as horizontal fringes in the image.

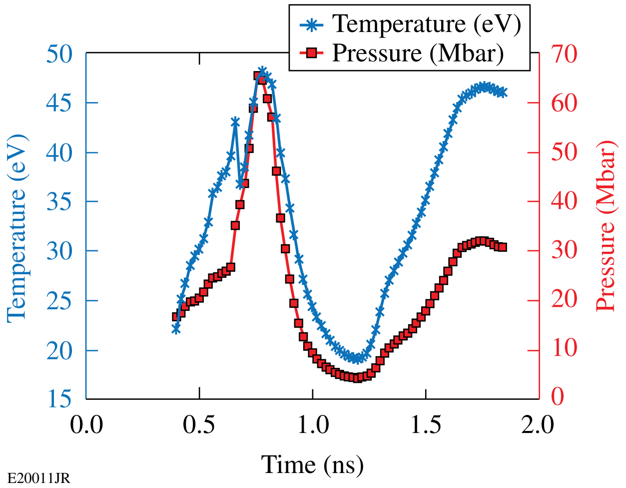

Figure 128.12
Simulated temperature (blue stars) and pressure (red squares) profiles of the $D_2$ shock front of the planar cryogenic target from *DRACO*. The shocked $D_2$ density reaches 3 to $4\times$ the initial liquid-$D_2$ density (0.171 g/cc) with pressures ranging from 15 to 25 Mbar and temperatures from 20 to 30 eV during the shock transit into the $D_2$ liquid. At 0.8 ns, the $D_2$ layer achieves its peak pressure of 65 Mbar at a temperature of 50 eV as a result of the rarefaction wave heating from the rear $CH_2$ window.

## Experimental Results

Figure 128.13 shows the measured modulation optical depth of the planar cryogenic target in Fig. 128.9 seeded with a 60-$\mu$m-wavelength preimposed mass modulation with an initial amplitude of 0.25 $\mu$m. The target was driven by a 2-ns square pulse with an intensity of $4 \times 10^{14}$ W/cm$^2$ [Fig. 128.13(a)]. The measured modulation amplitude(blue diamonds) are overplotted with the prediction from the 2-D hydrodynamics simulation *DRACO* (red line) showing relatively good agreement [Fig. 128.13(b)]. The measurement and simulation include contributions from both the front and rear plastic windows of

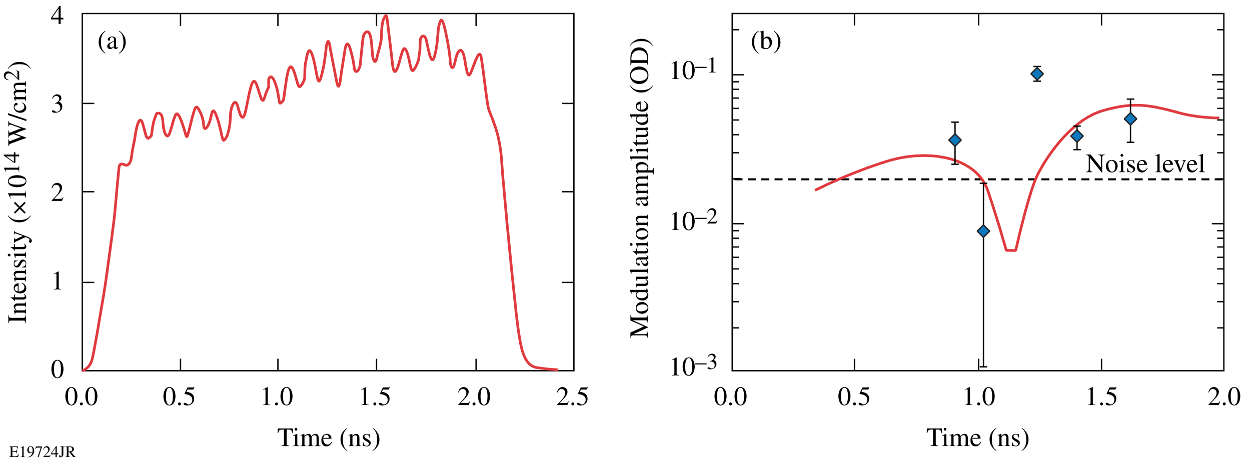

Figure 128.13
(a) The planar cryogenic target in Fig. 128.9 is driven by 12 overlapping drive beams with a 2-ns square pulse at a peak intensity of $4 \times 10^{14}$ W/cm$^2$. (b) The measured modulation amplitude is plotted (blue diamonds) as well as the prediction by *DRACO* using flux-limited thermal transport (red line) showing relatively good agreement.

the target up to ~1.2 ns, when the front window is ablated. The target acceleration begins at ~1.4 ns, so the modulation signal up to this time is dominated by the oscillating ablative RM instability,[25] observed as the large oscillating feature in the simulation. This characteristic of the ablative RM instability has been experimentally observed by U. Aglitskiy *et al.*[42,43] and O. Gotchev *et al.*[44,45] in pure-CH targets. After ~1.2 ns, simulation and measurements are dominated by the feedthrough modulations in the rear 8-$\mu$m $CH_2$ window, which are related to the modulation at the $D_2$ ablation front by Eq. (3).

## Discussion

The experiment demonstrates that *DRACO* closely reproduces the experiment using flux-limited local electron transport at an intensity of $4 \times 10^{14}$ W/cm$^2$. The large discrepancy between the experiment and simulation at the data point at 1.25 ns is likely the result of a difference between the experimental and simulated mass-ablation rates. Early in the drive ($t \ll 1.2$ ns), both the experimental and simulated optical depths include contributions from the front and rear plastic windows, while later in the drive ($t \gg 1.2$ ns) the front window is completely ablated, leaving only the rear window as the optical-depth contributor. In these regions, a small difference in ablation velocity between experiment and simulation could exist without disagreement in measured and simulated optical depths as a result of the slow growth observed in the target. Measurements taken as the front window is being completely ablated away ($t \sim 1.2$ ns) would show a larger discrepancy. In this case, if the simulated ablation velocity is greater than the experimental ablation velocity, the measurement at 1.25 ns would include contributions from both the front and rear windows, while the simulation includes only the rear window, contributing to the difference between experiment and simulation for that data point. In the other temporal regions, the simulation reproduces the behavior of the modulation evolution in this complex target, indicating that the measured hydrodynamic stability characteristics of $D_2$ are close to those predicted through theory and simulation.

Signal levels can be increased by designing an experiment with a longer pulse duration, causing the modulation to grow to larger amplitudes or decreasing the distance between the $D_2$ ablation front and the rear $CH_2$ window of the target, while still keeping a thick-enough $D_2$ layer such that the hydrodynamics of $D_2$ are relevant to the measurement. Noise is dominated by x-ray photon statistics as a result of condensation on the windows of the target, resulting in large-scale features with low x-ray transmissions. This effect was significantly reduced by the use of a target shroud and selective image analysis, although it remains the dominate noise contributor.

An alternative radiography approach to that presented here is the use of charged particles or low-energy x rays to directly measure the modulation evolution at the $D_2$ ablation front as well as the front and rear plastic windows. Targets designed for this approach would use thinner plastic windows that would directly measure the modulation evolution in the $D_2$ layer, allowing for higher-confidence comparisons between experiment and simulation.

## Conclusion

A direct-drive, RT experiment with a planar cryogenic-$D_2$ target was performed at the Omega Laser Facility. These are the first RT measurements in $D_2$ at conditions relevant to ICF using a mass-preimposed initial modulation. A planar cryogenic target was seeded with a 60-$\mu$m-wavelength mass modulation and driven with a 2-ns square pulse with a peak intensity of $4 \times 10^{14}$ W/cm$^2$ and radiographed using 1.3-keV x rays from a uranium backlighter. Experimental measurements showed reasonable agreement with the 2-D hydrodynamics code *DRACO*.

## ACKNOWLEDGMENT

This work was supported by the U.S. DOE Office of Inertial Confinement Fusion under Cooperative Agreement No. DE-FC52-08NA28302, the University of Rochester, and the New York State Energy Research and Development Authority. The support of DOE does not constitute an endorsement by DOE of the views expressed in this article.

## REFERENCES

1. S. Atzeni and J. Meyer-ter-Vehn, *The Physics of Inertial Fusion: Beam Plasma Interaction, Hydrodynamics, Hot Dense Matter*, International Series of Monographs on Physics (Clarendon Press, Oxford, 2004).
2. J. D. Lindl, *Inertial Confinement Fusion: The Quest for Ignition and Energy Gain Using Indirect Drive* (Springer-Verlag, New York, 1998).
3. Lord Rayleigh, Proc. London Math Soc. **XIV**, 170 (1883).
4. G. Taylor, Proc. R. Soc. London Ser. A **201**, 192 (1950).
5. S. E. Bodner, Phys. Rev. Lett. **33**, 761 (1974).
6. B. A. Remington *et al.*, Phys. Rev. Lett. **73**, 545 (1994).
7. S. G. Glendinning, S. N. Dixit, B. A. Hammel, D. H. Kalantar, M. H. Key, J. D. Kilkenny, J. P. Knauer, D. M. Pennington, B. A. Remington, R. J. Wallace, and S. V. Weber, Phys. Rev. Lett. **78**, 3318 (1997).
8. J. Grun *et al.*, Phys. Rev. Lett. **58**, 2672 (1987).
9. K. Shigemori *et al.*, Phys. Rev. Lett. **78**, 250 (1997).
10. H. Azechi *et al.*, Phys. Plasmas **4**, 4079 (1997).
11. C. J. Pawley *et al.*, Phys. Plasmas **6**, 565 (1999).
12. J. P. Knauer, R. Betti, D. K. Bradley, T. R. Boehly, T. J. B. Collins, V. N. Goncharov, P. W. McKenty, D. D. Meyerhofer, V. A. Smalyuk, C. P. Verdon, S. G. Glendinning, D. H. Kalantar, and R. G. Watt, Phys. Plasmas **7**, 338 (2000).
13. H. Azechi *et al.*, Phys. Rev. Lett. **98**, 045002 (2007).
14. V. A. Smalyuk, T. R. Boehly, D. K. Bradley, V. N. Goncharov, J. A. Delettrez, J. P. Knauer, D. D. Meyerhofer, D. Oron, and D. Shvarts, Phys. Rev. Lett. **81**, 5342 (1998).
15. M. M. Marinak *et al.*, Phys. Plasmas **5**, 1125 (1998).
16. V. A. Smalyuk, O. Sadot, J. A. Delettrez, D. D. Meyerhofer, S. P. Regan, and T. C. Sangster, Phys. Rev. Lett. **95**, 215001 (2005).
17. V. A. Smalyuk, O. Sadot, R. Betti, V. N. Goncharov, J. A. Delettrez, D. D. Meyerhofer, S. P. Regan, T. C. Sangster, and D. Shvarts, Phys. Plasmas **13**, 056312 (2006).
18. W. W. Hsing *et al.*, Phys. Plasmas **4**, 1832 (1997).
19. D. L. Tubbs, C. W. Barnes, J. B. Beck, N. M. Hoffman, J. A. Oertel, R. G. Watt, T. Boehly, D. Bradley, P. Jaanimagi, and J. Knauer, Phys. Plasmas **6**, 2095 (1999).
20. C. Cherfils *et al.*, Phys. Rev. Lett. **83**, 5507 (1999).
21. S. G. Glendinning *et al.*, Phys. Plasmas **7**, 2033 (2000).
22. V. A. Smalyuk, V. N. Goncharov, J. A. Delettrez, F. J. Marshall, D. D. Meyerhofer, S. P. Regan, and B. Yaakobi, Phys. Rev. Lett. **87**, 155002 (2001).
23. V. A. Smalyuk, S. B. Dumanis, F. J. Marshall, J. A. Delettrez, D. D. Meyerhofer, S. P. Regan, T. C. Sangster, B. Yaakobi, and J. A. Koch, Phys. Plasmas **10**, 830 (2003).
24. R. Betti, V. N. Goncharov, R. L. McCrory, and C. P. Verdon, Phys. Plasmas **5**, 1446 (1998).
25. V. N. Goncharov, Phys. Rev. Lett. **82**, 2091 (1999).
26. J. G. Wouchuk and K. Nishihara, Phys. Plasmas **3**, 3761 (1996).
27. P. W. McKenty, V. N. Goncharov, R. P. J. Town, S. Skupsky, R. Betti, and R. L. McCrory, Phys. Plasmas **8**, 2315 (2001).
28. C. P. Verdon, Bull. Am. Phys. Soc. **38**, 2010 (1993).
29. B. A. Remington *et al.*, Phys. Plasmas **22**, 241 (1995).
30. S. G. Glendinning, Bull. Am. Phys. Soc. **36**, 2375 (1991).
31. Y. Lin, T. J. Kessler, and G. N. Lawrence, Opt. Lett. **20**, 764 (1995).
32. S. Skupsky, R. W. Short, T. Kessler, R. S. Craxton, S. Letzring, and J. M. Soures, J. Appl. Phys. **66**, 3456 (1989).
33. V. Smalyuk, T. Boehly, and J. Knauer, Laboratory for Laser Energetics, private communication (2005).
34. D. G. Stearns *et al.*, Rev. Sci. Instrum. **57**, 2455 (1986).
35. R. Betti, V. Lobatchev, and R. L. McCrory, Phys. Rev. Lett. **81**, 5560 (1998).
36. P. B. Radha, T. J. B. Collins, J. A. Delettrez, Y. Elbaz, R. Epstein, V. Yu. Glebov, V. N. Goncharov, R. L. Keck, J. P. Knauer, J. A. Marozas, F. J. Marshall, R. L. McCrory, P. W. McKenty, D. D. Meyerhofer, S. P. Regan, T. C. Sangster, W. Seka, D. Shvarts, S. Skupsky, Y. Srebro, and C. Stoeckl, Phys. Plasmas **12**, 056307 (2005).
37. V. A. Smalyuk, T. R. Boehly, D. K. Bradley, J. P. Knauer, and D. D. Meyerhofer, Rev. Sci. Instrum. **70**, 647 (1999).

38. L. Spitzer, Jr. and R. Härm, Phys. Rev. **89**, 977 (1953).

39. R. C. Malone, R. L. McCrory, and R. L. Morse, Phys. Rev. Lett. **34**, 721 (1975).

40. S. P. Lyon and J. D. Johnson, Los Alamos National Laboratory, Los Alamos, NM, Report LA-UR-92-3407, NTIS Order No. DE85014241 (1992).

41. S. X. Hu, B. Militzer, V. N. Goncharov, and S. Skupsky, Phys. Rev. Lett. **104**, 235003 (2010).

42. Y. Aglitskiy *et al.*, Phys. Rev. Lett. **87**, 265001 (2001).

43. Y. Aglitskiy *et al.*, Phys. Plasmas **9**, 2264 (2002).

44. O. Gotchev, "Experiments on Dynamic Overpressure Stabilization of the Ablative Richtmyer–Meshkov Instability in ICF Targets," Ph.D. thesis, University of Rochester, 2004.

45. V. N. Goncharov, O. V. Gotchev, R. L. McCrory, P. W. McKenty, D. D. Meyerhofer, T. C. Sangster, S. Skupsky, and C. Cherfils-Clérouin, J. Phys. IV France **133**, 123 (2006).